Applied Catalysis B: Environmental 320 (2023) 121989

Contents lists available at ScienceDirect

Applied Catalysis B: Environmental

journal homepage: www.elsevier.com/locate/apcatb

Defects engineering of metal-organic framework immobilized Ni-La(OH)$_3$ nanoparticles for enhanced hydrogen production

Jianjun Long, Qilu Yao *, Xiaolei Zhang, Haochong Wu, Zhang-Hui Lu *

Institute of Advanced Materials (IAM), National Engineering Research Center for Carbohydrate Synthesis, Key Lab of Fluorine and Silicon for Energy Materials and Chemistry of Ministry of Education, College of Chemistry and Chemical Engineering, Jiangxi Normal University, Nanchang 330022, China

ARTICLE INFO

Keywords:
Hydrous hydrazine
Hydrazine borane
Dehydrogenation
Metal-organic framework
Defect

ABSTRACT

The development of low-cost, efficient, and durable catalysts to boost hydrogen production from hydrous hydrazine ($N_2H_4{\cdot}H_2O$) and hydrazine borane ($N_2H_4BH_3$) is critical, but still a huge challenge. Herein, for the first time, noble-metal-free La(OH)$_3$-doped Ni nanoparticles (NPs) supported on defect-rich metal−organic framework were constructed via a facile, green, and low-cost wet-chemical method. It is first found that the number of defects in MIL-125(Ti) can be easily regulated by a simple but efficient method. As a result, the defect-rich MIL-125-supported Ni-La(OH)$_3$ catalyst shows superior catalytic activity, 100 % H_2 selectivity, and robust durability for $N_2H_4{\cdot}H_2O$ dehydrogenation with NaOH at 343 K, providing a turnover frequency (TOF) value high up to 870 h^{-1}, surpassing all the non-noble metal catalysts reported so far and even outperforming some noble metal-containing catalysts. Interestingly, the catalyst also shows excellent catalytic efficiency for hydrogen production from $N_2H_4BH_3$ with a TOF value as high as 2381 h^{-1} at 343 K. The superior catalytic efficiency is mainly due to the existence of abundant defective MIL-125, electron-rich, good dispersed and small Ni NPs, as well as the synergistic effect between metal and support. This work delivers inspiration in defect engineering and provides a promising strategy for rationally designing high-efficiency MOFs-based catalysts for hydrogen generation and other heterogeneous catalysis.

1. Introduction

The heavy usage of fossil energy such as coal, oil and gas has brought many problems to energy and environment of the current society [1,2]. It is very necessary to find new energy to solve the above problems. Hydrogen is widely regarded as a potential hydrogen carrier due to its advantages of high energy density, wide sources, and no pollution [3–12]. However, the efficient and safe storage, transportation and release of hydrogen greatly hinder the realization of a hydrogen economic society. Hydrous hydrazine ($N_2H_4{\cdot}H_2O$), as a liquid hydrogen source, has attracted much attention by researchers because of its characteristics of high hydrogen content (8.0 wt%), convenient storage, and good stability [13–18]. Under suitable catalysts and reaction conditions, N_2H_4 can be completely decomposed into H_2 and N_2 (Eq. 1) [19–22]. However, if the catalysts and/or reaction conditions are not appropriate, the decomposition of N_2H_4 will also take place in another route (Eq. 2) [23,24], namely decomposition into N_2 and NH_3, which not only reduces the hydrogen production efficiency, but also poisons the catalyst. Thus, it is very important to develop a highly selective, efficient and stable catalyst to achieve complete dehydrogenation of N_2H_4.

$$N_2H_4(1) \rightarrow N_2(g) + 2H_2(g) \quad (1)$$

$$3N_2H_4(1) \rightarrow 4NH_3(g) + N_2(g) \quad (2)$$

Up to now, a variety of Ni-based catalysts have been widely developed for hydrogen production from $N_2H_4{\cdot}H_2O$ [25–34]. Among them, Ni-based catalysts containing precious metals (e.g., Pt, Rh, Ir, Pd) are considered to be highly active catalysts for this dehydrogenation reaction [35–39], yet the low reserves and high cost of precious metals hinder their widespread application. Therefore, tremendous efforts have been devoted to developing low-cost and abundant reserves of non-noble metal catalysts for $N_2H_4{\cdot}H_2O$ dehydrogenation [40–43]. Over the past decade, many methods have been used to optimize the catalytic activity of non-noble metal catalysts, including adjusting the composition, size, shape, structure, and so on [44–47]. Despite the progress already made, non-noble metal catalysts still have a certain gap in the catalytic activity compared to those of catalysts containing precious metals [48,49]. Thus, it is urgent to develop new strategies to further

* Corresponding authors.
E-mail addresses: yaoqilu@jxnu.edu.cn (Q. Yao), luzh@jxnu.edu.cn (Z.-H. Lu).

https://doi.org/10.1016/j.apcatb.2022.121989
Received 29 July 2022; Received in revised form 10 September 2022; Accepted 13 September 2022
Available online 14 September 2022

enhance the catalytic performance of the noble-metal free catalysts for $N_2H_4{\cdot}H_2O$ dehydrogenation, but it is also extremely challenging.

Metal-organic frameworks (MOFs), as a kind of porous crystalline materials rising in recent years, have attracted intense attention in a variety of applications, especially in catalysis, owing to their high surface areas and porosity, structural diversity, tailorable functionality [50–53]. Their permanent porosity enables them an inherent advantage in the anchoring metal NPs, which can effectively reduce the agglomeration of metal NPs and improve their dispersion, thereby increasing the quantity number of active sites and enhancing the performance of catalyst [23,35,36]. Another effective way to improve the catalytic performance is to tune the electronic structure of active sites by introducing defects or dopants [54,55]. In fact, the introduction of defects in MOFs not only serve as potential active sites to immobilize metal NPs and modulate the electronic state of metal NPs, but also helps in overcoming diffusion limitations. Moreover, MOFs with rich defects make the adsorption and activation of reactants more easily, which may further improve the catalytic activity [56]. Therefore, it is very attractive to promote performance of catalyst by regulating defects of MOFs, however, which still has rarely been reported in the dehydrogenation of nitrogen hydrides yet. Recently, defect engineering of MOFs has become a research hotspot because it leads to a diversity of materials [57]. Various methods have been developed to design defects, such as modulator approaches and thermal activation strategies [58]. However, currently reported preparation methods are still relatively few and complex. Therefore, there is an urgent need to develop a simple but effective method.

Herein, for the first time, noble-metal-free $La(OH)_3$-doped Ni NPs immobilized on defect-rich porous MIL-125 (Ni-$La(OH)_3$/D-MIL-125) were fabricated by a simple, green, and low-cost wet-chemical method. Ultrafine Ni-$La(OH)_3$ NPs with a mean particle size of about 1.8 nm were highly dispersed on D-MIL-125. The defects in catalysts were generated during the chemical reduction procedure, with which partial Ti(IV) in some Ti-O clusters of MIL-125 can be reduced to Ti(III) by $NaBH_4$. At the same time, Ti(III) is easily oxidized and further converted to Ti(IV). Due to the interconversion between Ti(IV) and Ti(III), a large number of defects will be formed in MIL-125, which may be conducive to the optimization of the electronic structure of the catalyst and expose more active sites. Moreover, MOFs with rich defects make the adsorption and activation of reactants more easily, which may further improve the catalytic activity. Unexpectedly, the resultant Ni-$La(OH)_3$/D-MIL-125 catalyst showed extremely high catalytic performance, 100% H_2 selectivity, and remarkable robust durability for $N_2H_4{\cdot}H_2O$ dehydrogenation with NaOH. The TOF value of Ni-$La(OH)_3$/D-MIL-125 for dehydrogenation of $N_2H_4{\cdot}H_2O$ is calculated to be 870 h^{-1} at 343 K, which stands at the highest level among all the non-noble-metal catalysts reported so far. In addition, the Ni-$La(OH)_3$/D-MIL-125 catalyst also showed an outstanding catalytic efficiency for dehydrogenation of $N_2H_4BH_3$ with a TOF value of 2381 h^{-1} at 343 K. The development of efficient, stable, and low-cost catalysts has accelerated the practical utilization of $N_2H_4{\cdot}H_2O$ and $N_2H_4BH_3$ as efficient hydrogen suppliers in fuel cells.

2. Experimental section

2.1. Synthesis of catalysts

2.1.1. Syntheses of Ni-La(OH)$_3$/D-MIL-125

MIL-125 was synthesized following the previously reported procedure with some changes [59], see the Supporting information for details. The synthesis of Ni-$La(OH)_3$/D-MIL-125 was prepared through a facile, green, and low-cost wet-chemical method at 298 K. Typically, activated MIL-125 (70 mg) was dispersed in 5 mL deionized water, then 48.4 mg of $NiCl_2{\cdot}6\,H_2O$ (0.2 mmol) and 8.7 mg of $La(NO_3)_30.6\,H_2O$ (0.02 mmol) were added to the MIL-125 suspension and sonicated for 30 min at 298 K. After that, quickly add 70 mg of $NaBH_4$ to the above mixture and stir vigorously. Finally, the black product of Ni-$La(OH)_3$/D-MIL-125 (9.1 mol% La) was obtained until the bubble generation ceased. The Ni-$La(OH)_3$/D-MIL-125 catalysts reduced by different amounts of $NaBH_4$ (10, 30, 50, and 90 mg) were also synthesized and denoted as Ni-$La(OH)_3$/D-MIL-125-x (x represents the amounts of $NaBH_4$).

For comparison, support-free Ni, Ni-$La(OH)_3$, and Ni/D-MIL-125 samples were prepared by a similar method, except without adding MIL-125 and/or $La(NO_3)_3$. The physical mixture of Ni-$La(OH)_3$ and D-MIL-125 (Ni-$La(OH)_3$ + D-MIL-125) and the physical mixture of Ni-$La(OH)_3$ and MIL-125 (Ni-$La(OH)_3$ + MIL-125) were prepared by directly mixing Ni-$La(OH)_3$ NPs with D-MIL-125 or MIL-125, where D-MIL-125 was obtained by treating MIL-125 with 70 mg of $NaBH_4$. The Ni-$La(OH)_3$ NPs immobilized by other supports were synthesized following a similar procedure to Ni-$La(OH)_3$/D-MIL-125, except that ZIF-67, ZIF-8, and UiO-66 were used instead of MIL-125.

2.2. Catalytic activity measurement

Typically, the catalytic reactions were carried out in a 50 mL round-bottom flask containing uniformly dispersed synthetic Ni-$La(OH)_3$/D-MIL-125 catalyst and NaOH (3.0 M, 5 mL). The reaction flask was then taken on a heated stirrer with the temperature set to 343 K. Subsequently, $N_2H_4{\cdot}H_2O$ (2 mmol) or $N_2H_4BH_3$ (1 mmol) was added to the reactor, and the reaction started under vigorous stirring. Before measuring the gas produced by the dehydrogenation reaction, the gas was passed through a trap containing a solution of HCl (1.0 M). The catalytic activities of other catalysts for $N_2H_4{\cdot}H_2O$ dehydrogenation were also applied to the same method. The molar number of Ni for all the catalytic reactions was kept at 0.2 mmol. The H_2 selectivity for $N_2H_4{\cdot}H_2O$ (α) and $N_2H_4BH_3$ (β) dehydrogenation is calculated by the following reaction formulas (Eqs. (3)–(6)):

$$N_2H_4 \rightarrow 2\alpha H_2 + (2\alpha{+}1)/3N_2 + 4(1{-}\alpha)/3NH_3 \quad (3)$$

$$N_2H_4BH_3 + 3\,H_2O \rightarrow B(OH)_3 + (3 + 2\beta)\,H_2 + (2\beta{+}1)/3\,N_2 + 4(1{-}\beta)/3NH_3 \quad (4)$$

$$\alpha = \frac{3x\text{-}1}{8} \quad \left[x = \frac{n(H_2 + N_2)}{n(N_2H_4)} \quad \left(\frac{1}{3} \leq x \leq 3\right)\right] \quad (5)$$

$$\beta = \frac{3\lambda - 10}{8} \quad \left[\lambda = \frac{n(H_2 + N_2)}{n(N_2H_4BH_3)} \quad \left(\frac{10}{3} \leq \lambda \leq 6\right)\right] \quad (6)$$

For the cycle test, after one cycle of the decomposition reaction was completed, an equal amount of $N_2H_4{\cdot}H_2O$ (2 mmol) or $N_2H_4BH_3$ (1 mmol) was subsequently injected into the reaction flask. The cycle test was repeated twenty times at 343 K. After twenty cycles, the catalyst was washed three times with deionized water, centrifuged and dried at 333 K, and then used for XRD and TEM analysis.

3. Results and discussion

3.1. Catalysts characterization

Defect-rich MIL-125-supported Ni-$La(OH)_3$ (denoted as Ni-$La(OH)_3$/D-MIL-125) were prepared by a facile and green reduction method, as illustrated in Scheme 1. First, activated MIL-125 was dispersed in deionized water, then $NiCl_2{\cdot}6H_2O$ and $La(NO_3)_30.6H_2O$ were added to the MIL-125 suspension, and sonicated at 298 K for 30 min. Afterwards, various dosages of $NaBH_4$ (10–90 mg) were added to the above mixture under vigorous stirring to finally obtained the black product of Ni-$La(OH)_3$/D-MIL-125-x (x represents the amounts of $NaBH_4$). The Ni-$La(OH)_3$/D-MIL-125-x were used as catalysts for hydrogen production from $N_2H_4{\cdot}H_2O$. The Ni-$La(OH)_3$/D-MIL prepared with 70 mg $NaBH_4$ showed the best catalytic activity among all the synthesized catalysts (vide infra). Therefore, if the catalyst does not indicate the amount of reducing agent in the article, it refers to the synthetic with 70 mg of $NaBH_4$.

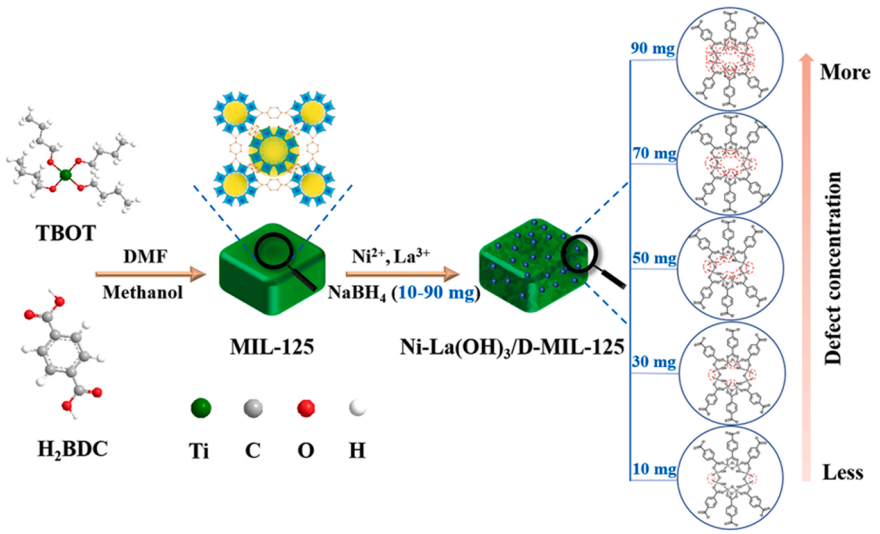

Scheme 1. Schematic illustration for the synthesis of Ni-La(OH)$_3$/D-MIL-125 reduced with different $NaBH_4$ dosages.

The crystal structures of the parent MIL-125 and Ni-La(OH)$_3$/D-MIL-125-x (x = 10–90 mg) were characterized by X-ray diffraction (XRD). As depicted in Fig. 1a, the XRD pattern of the parent MIL-125 structure is in good agreement with its simulated XRD pattern, indicating that MIL-125 was synthesized successfully. As can be noticed, the XRD patterns of Ni-La(OH)$_3$/D-MIL-125-x (x = 10–70 mg) were identical to that of the parent MIL-125, implying that their structures were maintained well after the defect introduction. However, with the amounts of $NaBH_4$ increased from 10 mg to 70 mg, the diffraction peaks intensity of MIL-125 gradually decreased, indicating that the long-range order of the

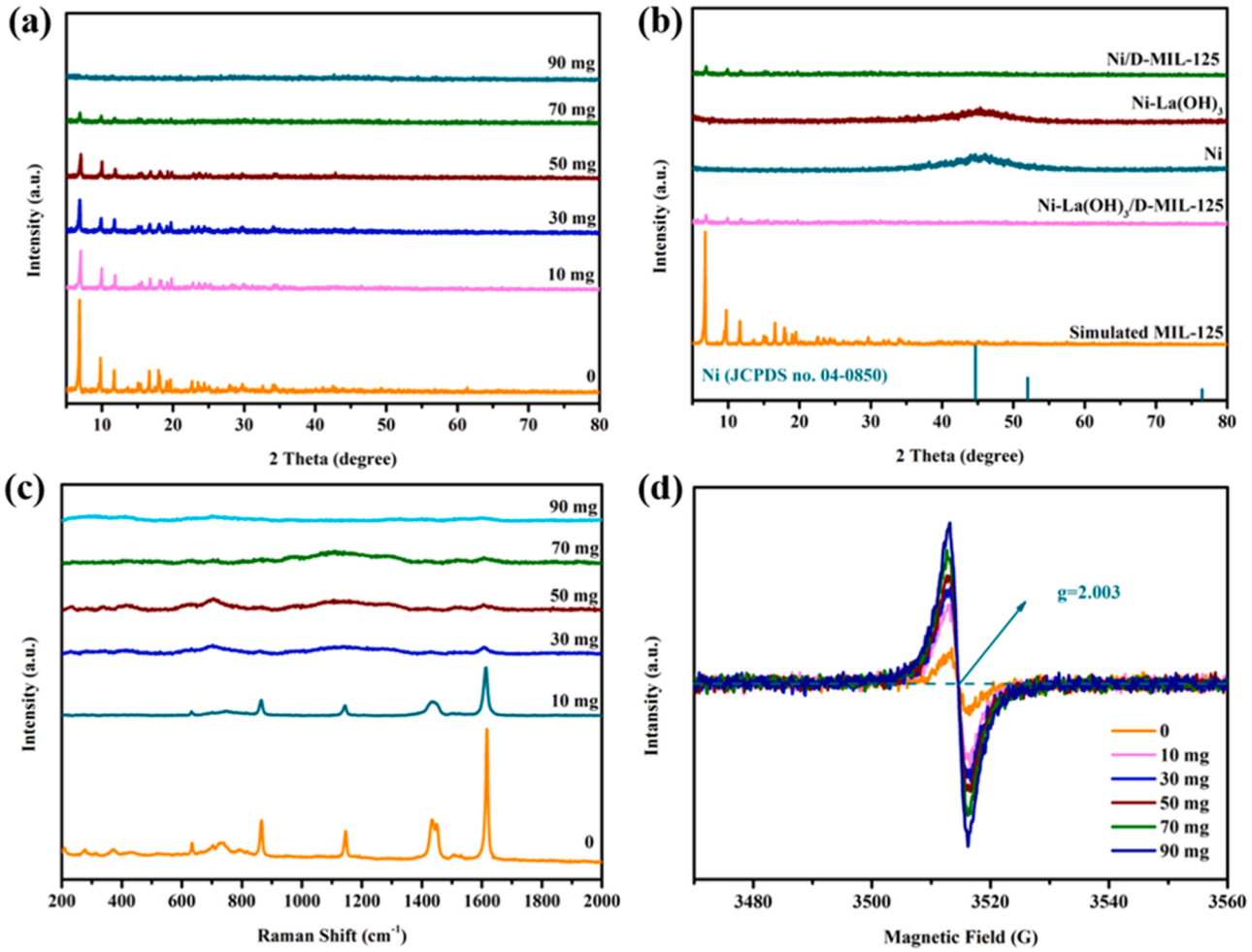

Fig. 1. XRD patterns of (a) Ni-La(OH)$_3$/D-MIL-125-x (x = 10–90 mg) prepared with different $NaBH_4$ dosages and (b) Ni, Ni-La(OH)$_3$, Ni/D-MIL-125, La(OH)$_3$/D-MIL-125, and Ni-La(OH)$_3$/D-MIL-125. (c) Raman spectra and (d) EPR spectra of Ni-La(OH)$_3$/D-MIL-125-x (x = 10–90 mg) prepared with different $NaBH_4$ dosages.

lattice reduced, the crystallite dimension decreased, and the defect concentration gradually increased. When $NaBH_4$ was continuously increased to 90 mg, the diffraction peak of MIL-125 disappeared completely, implying the amorphization of the Ni-La$(OH)_3$/D-MIL-125–90 sample. Such crystallinity change may be caused by the introduction of $NaBH_4$, which can reduce Ti(IV) to Ti(III) of the Ti-O cluster of MIL-125(Ti). Additionally, the Ti(III) is easily oxidized and further converted to Ti(IV). The interconversion between Ti(IV) and Ti(III) during the reduction process is further evidenced by the color change of the MIL-125 suspension. As shown in Fig. S1, after the addition of $NaBH_4$, the white MIL-125 suspension turned dark blue and finally white again. During the conversion of Ti(IV) to Ti(III), a large number of defects will be formed, which is similar to previous literature reports [60]. Thus, the XRD results confirm that the modulation of defects engineering of Ni-La$(OH)_3$/D-MIL-125-*x* can be achieved by simply changing the amount of the reductant agent $NaBH_4$. It should be noted that Ni-La$(OH)_3$/D-MIL-125 and Ni/MIL-125 did not show any characteristic diffraction peaks related to Ni and/or La$(OH)_3$ species (Fig. 1b), which is possibly ascribed to the small size and nano-crystallinity structure (vide infra) of Ni and Ni-La$(OH)_3$ and their excellent dispersion on D-MIL-125. While for support-free Ni and Ni-La$(OH)_3$ NPs, there is a central peak obviously located at 44.5° (Fig. 1b), which is assigned to the (111) plane of face-centered cubic (fcc) Ni (JCPDS: 04–0850), indicating that Ni and Ni-La$(OH)_3$ have crystalline structures.

The structural characteristics and phase composition of the parent MIL-125 and Ni-La$(OH)_3$/D-MIL-125-*x* (x = 10–90 mg) catalysts were further investigated by Raman spectroscopy. As shown in Fig. 1c, six prominent peaks appeared at 633, 866, 1145, 1433, 1449 and 1616 cm^{-1}, which are the features of the vibration modes of organic ligands (H_2BDC) of Ti-based MOF. The results revealed that in addition to the vibrational modes of C-H and C═C bonds of the benzene ring, these bands also correspond to the asymmetric and symmetric vibrational modes of carboxylic acid groups, further confirming the successful synthesis of MIL-125(Ti) [61]. By contrast, the intensity of Raman peaks for Ni-La$(OH)_3$/D-MIL-125-*x* (x = 10–90 mg) gradually weakened with the increase of the amount of reducing agent $NaBH_4$, indicating its imperfectly ordered crystal structure as a result of increased oxygen deficiency. More evidence can also be found in electron paramagnetic resonance (EPR) spectra of pristine MIL-125 and series Ni-La$(OH)_3$/D--MIL-125-*x* (x = 10–90 mg). As presented in Fig. 1d, the EPR spectrum of the MIL-125(Ti) displays a negligible signal, which may be assigned to the inherent defects of MIL-125(Ti). While the Ni-La$(OH)_3$/D-MIL-125-*x* (x = 10–90 mg) exhibited symmetrical EPR signals located at g = 2.003, indicating the existence of a large number of uncoupled Ti(IV) centers, which serve as defects in the frameworks [62]. In addition, with the increase of the amount of reducing agent $NaBH_4$, a stronger EPR signal could be observed, which indicates that there are more defects existing in the crystal defects. The above results verify that the amount of $NaBH_4$ used in the catalyst reduction process can easily adjust the defect concentration.

Fourier transform infrared (FTIR) spectra were further performed to analyze the chemical structure of the synthesized catalysts. As shown in Fig. S2, the characteristic bands from 500 to 800 cm^{-1} were attributed to O-Ti-O vibrations, while the bands from 1400 to 1700 cm^{-1} were corresponded to carboxylates, which is consistent with previously reported results. [63,64]. For Ni-La$(OH)_3$/D-MIL-125-*x* (x = 10–70 mg), there was almost no significant change in the FTIR spectra of MIL-125, further indicating the structures of MIL-125 was well maintained. However, when the amount of reducing agent $NaBH_4$ further increased to 90 mg, the infrared absorption peaks of Ni-La$(OH)_3$/D-MIL-125–90 almost disappeared, indicating that the microstructure of MOF was almost completely destroyed, which was consistent with the results obtained in XRD pattern.

N_2 adsorption/desorption isotherms and pore size distribution of the as-prepared samples were illustrated in Fig. 2 and Fig. S3. For the pristine MIL-125 (Fig. 2a), a type I isotherm was observed, indicating a typical microporous structure. The BET surface of pristine MIL-125 was measured to be 1589 $m^2\ g^{-1}$, which is similar to the values previously literature [65]. When Ni-La$(OH)_3$ NPs were loaded on MIL-125, the shape of adsorption isotherms showed an intermediate mode between type I (microporous structure) and type IV (mesoporous structure). Meanwhile, the amount of N_2 adsorbed at a very low relative pressure ($P/P_0 < 0.1$) was clearly decreased with the amount of reduction agent increased, indicating that the microporosity of Ni-La$(OH)_3$/D-MIL-125-*x* (x = 10–90 mg) is significantly decreased, consistent with the micropore size distribution curves (Fig. 2b). Additionally, minor hysteresis loops are observed for Ni-La$(OH)_3$/D-MIL-125, indicating that these catalysts have mesoporous pores, as confirmed by the Barret-Joyner-Halenda (BJH) pore size distribution curves (Fig. S3). Based on the N_2 absorption–desorption analyses, the surface area of Ni-La$(OH)_3$/D-MIL-125 obtained by reduction with 10, 30, 50, 70, and 90 mg of $NaBH_4$ are 1310, 1147, 946, 638, and 339 $m^2\ g^{-1}$, respectively. As listed in Table S1, with the amount of reduction agent increased, the specific surface area and pore volume of Ni-La$(OH)_3$/D-MIL-125 decreased, and the average pore diameter increased due to the collapse and combination of pore structure. The above results indicate that abundant defects are formed in Ni-La$(OH)_3$/D-MIL-125-*x* (x = 10–90 mg) during the reduction process, consistent with the XRD, Raman, and EPR characterization results.

The morphology of the pristine MIL-125 and Ni-La$(OH)_3$/MIL-125-*x*

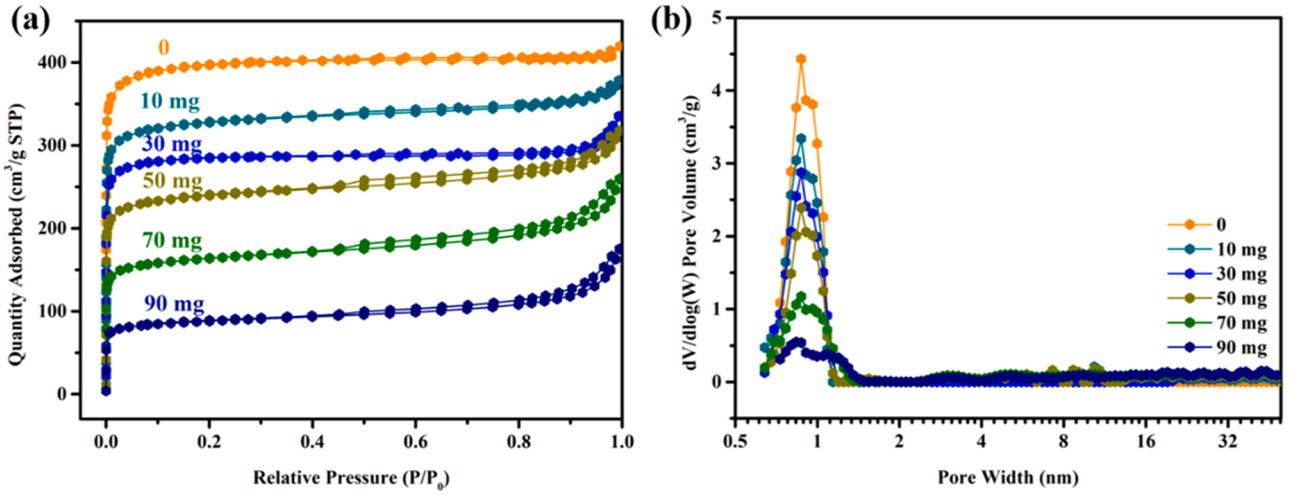

Fig. 2. (a) Nitrogen adsorption-desorption isotherms and (b) pore distribution of Ni-La$(OH)_3$/D-MIL-125-*x* (x = 10–90 mg) prepared with different $NaBH_4$ dosages.

(x = 10–90 mg) were observed by SEM and TEM. As displayed in Fig. 3a, the parent MIL-125 has a disc structure with a smooth surface and size range from 0.5 to 1.0 μm. After loading the Ni-La(OH)$_3$ NPs, the MOF framework of Ni-La(OH)$_3$/D-MIL-125 prepared by 10–70 mg $NaBH_4$ was well retained except for rough surface (Fig. 3b and Fig. S4). However, when the $NaBH_4$ dosage was increased to 90 mg, part of framework structure of Ni-La(OH)$_3$/MIL-125 was destroyed (Fig. S4d), agreeing with the previous XRD (Fig. 1a) and FTIR results (Fig. S2). TEM images confirmed that the framework of Ni-La(OH)$_3$/D-MIL-125 prepared by 70 mg of $NaBH_4$ was well maintained (Fig. 3d). Additionally, Ni-La(OH)$_3$ NPs were highly dispersed on the framework of MIL-125 (Fig. 3e-g). The mean size of Ni-La(OH)$_3$ NPs is about 1.8 nm (Fig. 3h), which is larger than the cavity of MIL-125 (~1.6 nm), indicating that Ni-La(OH)$_3$ NPs are located on the MIL-125 surface. The high-resolution TEM image of Ni-La(OH)$_3$/D-MIL-125 showed that the lattice fringe is 0.203 nm (Fig. 3i), which corresponds well with the lattice spacing of the face-centered cubic Ni (111) planes. Moreover, the selected area electron diffraction (SAED) pattern of Ni-La(OH)$_3$/D-MIL-125 indicated the low crystallinity of metallic Ni (inset of Fig. 3i). The EDX spectrum of Ni-La(OH)$_3$/D-MIL-125 (Fig. S5) exhibited that the molar ratio of $n_{La}/n_{(Ni+La)}$ is calculated to be 9.4%, which is close to the theoretical value 9.1%. Moreover, the corresponding EDS elemental mappings further confirmed the homogeneous dispersion of Ni, La, Ti, C, and O (Fig. 3j and k) in the Ni-La(OH)$_3$/D-MIL-125 sample. Similarly, Ni NPs (2.4 nm) without adding La(OH)$_3$ were also well dispersed on MIL-125 (Ni/D-MIL-125) (Figs. S6a-d). For free Ni-La(OH)$_3$ NPs without MIL-125, the average size of Ni NPs is about 2.7 nm, but it is easy to agglomerate together (Figs. S6e-h). In contrast, free Ni NPs have relatively large particle sizes (Fig. S6i-l). Therefore, the introduction of La(OH)$_3$ and D-MIL-125 is beneficial to forming small-sized and highly dispersed metal NPs to a certain extent.

X-ray photoelectron spectroscopy (XPS) after Ar sputtering were used to analyze the chemical states and electronic effects of Ni-La(OH)$_3$/D-MIL-125 and its comparative samples. The survey XPS spectra of Ni-La(OH)$_3$/D-MIL-125 (Fig. 4a) and MIL-125 (Fig. S7) show the presence of Ni, La, Ti, C, O and C, Ti, O, respectively, agreeing with the EDX result (Fig. S5). Fig. 4b displays that the peak of Ni $2p_{3/2}$ overlaps with that of La $3d_{3/2}$. Therefore, the spectra of Ni $2p_{3/2}$ and La $3d_{3/2}$ should be analyzed separately [66,67]. The Ni $2p_{1/2}$ of Ni-La(OH)$_3$/MIL-125 showed a peak at about 869.9 eV that was ascribed to metallic Ni(0). While the peak of Ni $2p_{1/2}$ in Ni-La(OH)$_3$/D-MIL-125 at 874.4 eV is assigned to the oxidized Ni, which is mainly caused by the surface oxidation of catalyst during XPS sample preparation (Fig. 4c) [68]. In addition, the Ni $2p_{1/2}$ peak at about 880.6 eV is corresponded to its satellite peaks (Fig. 4c). The binding energy for metallic Ni (869.9 eV) in Ni-La(OH)$_3$/D-MIL-125 was shifted to lower values compared with those of Ni-La(OH)$_3$ NPs (870.1 eV) and Ni/D-MIL-125 (870.3 eV), indicating that some electrons transferred from La(OH)$_3$ and D-MIL-125 to Ni (Fig. S8). This modified electronic structure in Ni-La(OH)$_3$/D-MIL-125 can promote the cleavage of N-H bond, thereby enhancing the performance of catalytic reaction [69]. As displayed in Fig. 4d, the La $3d_{5/2}$ peaks at 833.5 and 837.0 eV represent La(III) and its satellite peaks, respectively. The binding energy difference between the two peaks is 3.5 eV, indicating that La mainly exists in the form of La(OH)$_3$ [32,67]. As depicted in Fig. 4e, the Ti 2p spectrum of Ni-La(OH)$_3$/D-MIL-125 was deconvoluted into four peaks, corresponding to Ti(IV) (458.4 and

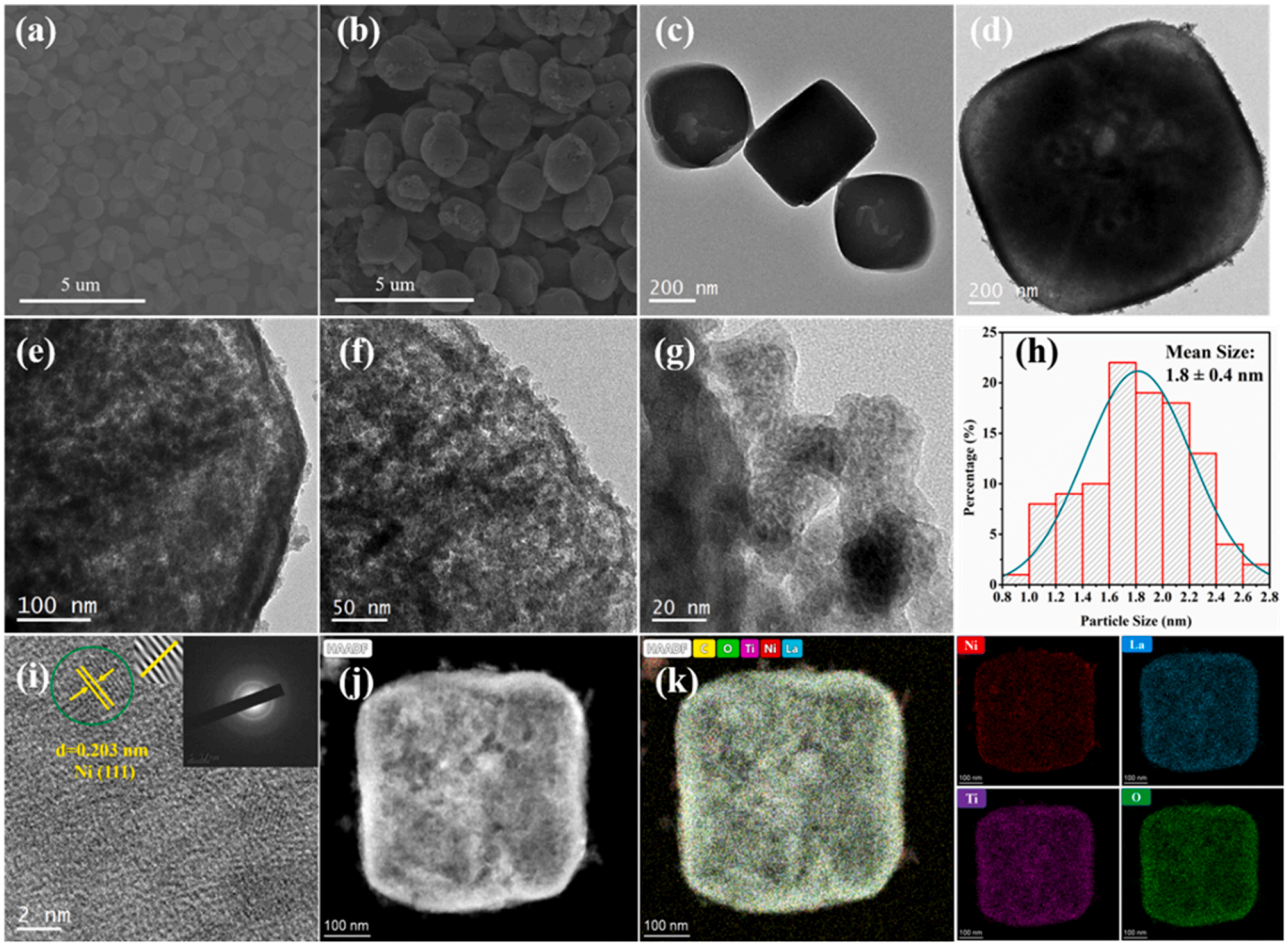

Fig. 3. SEM images of (a) MIL-125 and (b) Ni-La(OH)$_3$/D-MIL-125; (c) TEM image of MIL-125; (d-g) TEM images, (h) particle size distribution, (i) HRTEM image (inset SEAD image), (j) HAADF-STEM image of Ni-La(OH)$_3$/D-MIL-125 and (k) the corresponding EDX mapping images of Ni, La, Ti, and O.

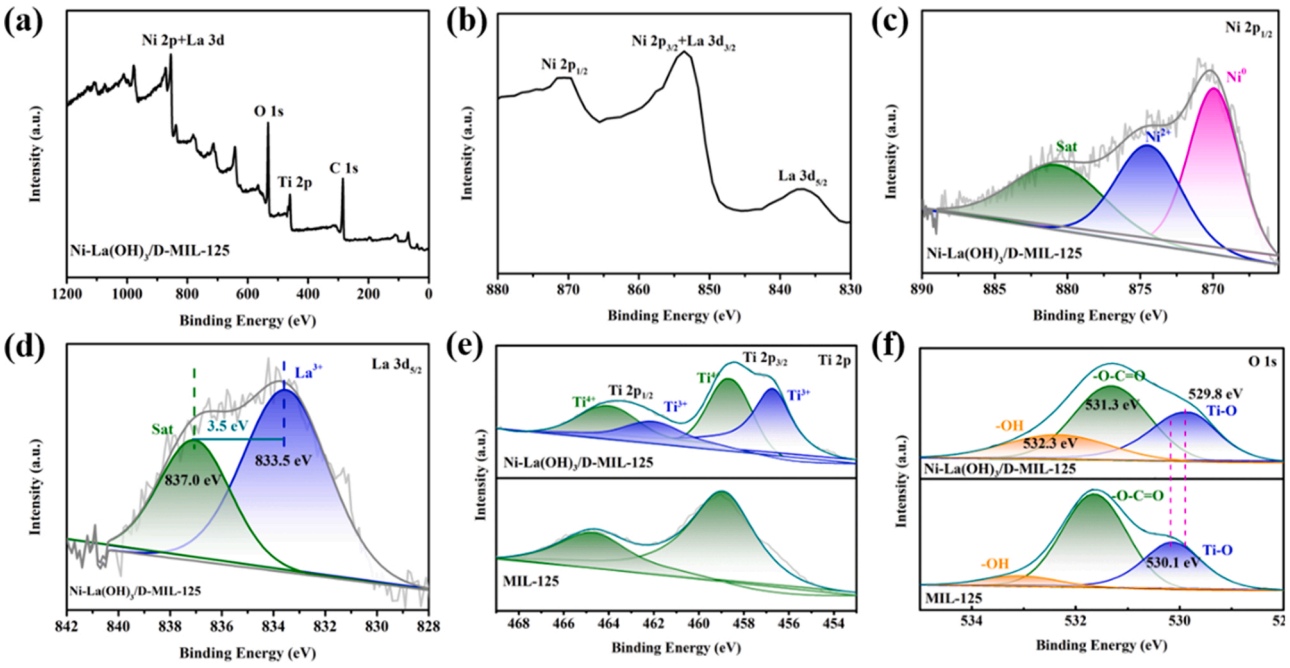

Fig. 4. The survey XPS spectrum of (a) Ni-La(OH)$_3$/D-MIL-125; The XPS spectra of (b) Ni 2p$_{3/2}$/La 3d$_{3/2}$, (c) Ni 2p$_{1/2}$, and (d) La 3d$_{5/2}$ for Ni-La(OH)$_3$/D-MIL-125; The XPS spectra of (e) Ti 2p and (f) O 1 s for MIL-125 and Ni-La(OH)$_3$/D-MIL-125.

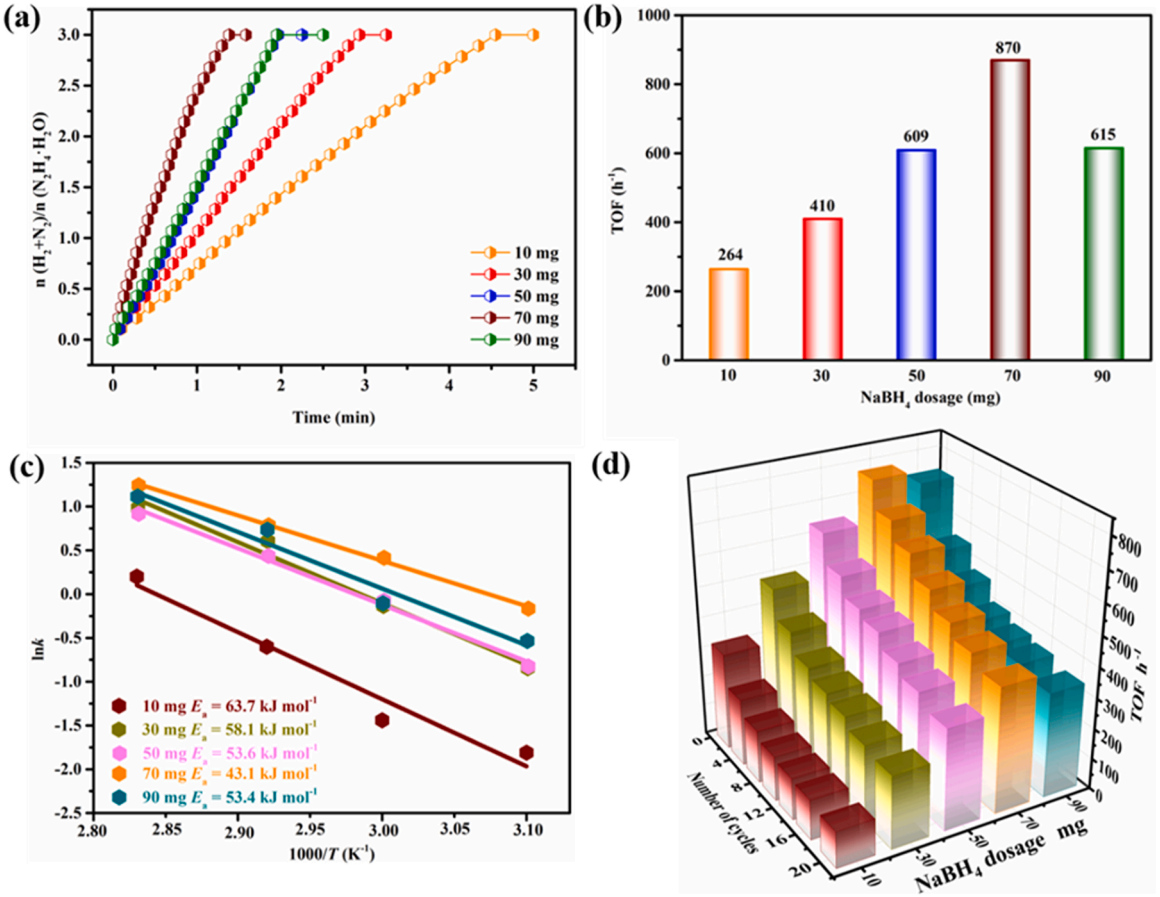

Fig. 5. (a) Time course plots for hydrogen evolution from aqueous N_2H_4 solution (0.4 M, 5 mL), (b) the corresponding the TOF values, (c) the related Arrhenius plot versus 1000/T, and (d) stability activities over Ni-La(OH)$_3$/D-MIL-125-*x* (*x* = 10–90 mg) prepared with different $NaBH_4$ dosages in the presence of NaOH (3.0 M) at 343 K ($n_{Ni}/N_2H_4·H_2O$ = 0.1).

464.0 eV) and Ti(III) (456.7 and 462.1 eV) species. In contrast, no peak of Ti(III) was observed in pristine MIL-125, indicating that Ti(III) was generated during the catalyst reduction process, which is completely consistent with the phenomenon in Fig. S1. The charge imbalance induced by Ti(III) promotes the formation of oxygen vacancies on the surface of catalyst. For the O 1s spectrum of the Ni-La$(OH)_3$/D-MIL-125 (Fig. 4f), the peak at 529.8 eV is attributed to the existence of Ti-O bond, while another two peaks at 531.3 and 532.3 eV can be corresponded to the carboxylate groups (-O-C═O) and surface absorbed oxygen (-OH), respectively. Additionally, compared with pristine MIL-125, the three peaks of O 1s in Ni-La$(OH)_3$/D-MIL-125 were negatively shifted, indicating that the chemical reduction caused the formation of abundant oxygen defects, which could have the potential to promote catalytic activity.

3.2. Catalytic activity

The catalytic activity of Ni-La$(OH)_3$/D-MIL-125-x (x = 10–90 mg) prepared with different amounts of reducing agent $NaBH_4$ for the dehydrogenation of $N_2H_4{\cdot}H_2O$ was evaluated in a typical water-filled graduated buret system. As displayed in Fig. 5a, the catalytic activity of catalysts is highly sensitive to the amount of reducing agent $NaBH_4$. When the Ni-La$(OH)_3$/D-MIL-125 prepared with a low amount of $NaBH_4$ (10 mg), the complete dehydrogenation of N_2H_4 at 343 K can finish in 4.5 min with a 100 % hydrogen selectivity and TOF of 264 h^{-1}. The catalytic performance of Ni-La$(OH)_3$/D-MIL-125 for N_2H_4 dehydrogenation can be further improved as the amount of reducing agent increases to 70 mg, indicating that the increase of catalyst defect content is beneficial to improving catalytic activity. However, when the amount of reducing agent further increases to 90 mg, the catalytic activity of Ni-La$(OH)_3$/MIL-125–90 decreased, which may be caused by the destruction of the partial framework structure of the catalyst (Fig. S4d). Clearly, the Ni-La$(OH)_3$/D-MIL-125 prepared with 70 mg of $NaBH_4$ showed the best catalytic performance, with 3.0 equivalents of (N_2 +H_2) can be released in only 1.38 min at 343 K with NaOH. Gas chromatography (GC) analysis showed that the produced gas contained only N_2 and H_2 (Fig. S9), indicating a 100 % H_2 selectivity for N_2H_4 dehydrogenation. The TOF over Ni-La$(OH)_3$/D-MIL-125–70 was calculated as high as 870 h^{-1}, exceeding all the non-noble metal catalysts reported so far, and even higher than some noble metal-containing catalysts. The outstanding catalytic activity is mainly due to the abundant defect sites, electron-rich and small-size Ni NPs, and the strong synergistic interaction between metal and support.

In order to deeply understand the effect of reductant dosage on the catalytic activity, kinetics experiments of the above catalysts toward N_2H_4 dehydrogenation at 323 − 353 K were carried out. As shown in Fig. S10, the hydrogen generation rate of all the Ni-La$(OH)_3$/D-MIL-125-x (x = 10–90 mg) catalysts increase significantly with the increase in temperature. Fig. 5c exhibits the corresponding Arrhenius plots (ln k vs. 1000/T) for the catalysts. By fitting the plots, the activation energy (E_a) for Ni-La$(OH)_3$/D-MIL-125 prepared with 10, 30, 50, 70, and 90 mg of $NaBH_4$ were calculated to be 63.7, 58.1, 53.6, 43.1, and 53.4 kJ mol^{-1}. The low activation energy value on Ni-La$(OH)_3$/D-MIL-125–70 is in good agreement with its optimal catalytic activity, which is lower than most reported values (Table S2), demonstrating a greatly enhanced reaction kinetics. The results further demonstrated that the generation of abundant defects effectively reduces the energy barrier of the reaction and improves the catalytic activity.

Besides the activity and kinetic behavior measurements, the stability evaluation of catalyst is another key criterion to be considered for its practical application. Herein, the durability of the catalysts prepared with different dosages of reduction agent $NaBH_4$ was evaluated to explore the effects of the dosage of $NaBH_4$ on the durability. To this end, the durability of each catalyst was evaluated up to 20 cycles (Fig. 5d and S11), in which an equal amount of $N_2H_4{\cdot}H_2O$ was added into the reaction flask after the previous run was completed. After 20 cycles, the H_2 selectivity of all catalysts was still retained at 100% (Fig. S11). However, the catalytic activity of all catalysts decreased gradually, and the decreasing rate was related to the dosage of reduction agent $NaBH_4$ and the trend is similar to the activity and kinetic behavior. When the Ni-La$(OH)_3$/D-MIL-125 catalyst prepared with a low amount of reducing agent $NaBH_4$ (e.g., 10 mg) showed severe deactivation, the activity remained at 37 % of the initial activity at the 20th cycle. As shown in Fig. 5d, it can be seen that the stability of Ni-La$(OH)_3$/D-MIL-125-x (x = 10–70 mg) is enhanced with the increase of the amount of reducing agent, the optimal amount of $NaBH_4$ is 70 mg, and the activity remained 53 % of the initial activity at the 20th cycle. After the durability test, the Ni-La$(OH)_3$/D-MIL-125–70 catalyst was separated from the solution for XRD and TEM characterization. As shown in Fig. S12, the diffraction peaks of Ni-La$(OH)_3$/D-MIL-125–70 disappeared after 20 cycles, which may be caused by the prolonged corrosion of MOF under alkaline conditions. However, the morphology of MIL-125 after 20 cycles was well retained and the Ni-La$(OH)_3$ NPs are still highly dispersed on the MIL-125, as verified by TEM image (Fig. S13).

The catalytic activities of the as-synthesized Ni-La$(OH)_3$/D-MIL-125 together with support-free Ni NPs, Ni-La$(OH)_3$ NPs, Ni/D-MIL-125, and metal-free La$(OH)_3$/D-MIL-125 for hydrogen production from N_2H_4 were also investigated. As shown in Fig. 6a, the support-free Ni NPs showed a low H_2 selectivity and activity for this dehydrogenation reaction, only generating 1.84 equiv. (N_2 +H_2) per $N_2H_4{\cdot}H_2O$ (α = 0.57) in about 120 min. After the Ni NPs were grown on the MIL-125 support or doped with La$(OH)_3$, the H_2 selectivity and catalytic activity were enhanced greatly, with which 3 and 2.2 equiv. (N_2 +H_2) per $N_2H_4{\cdot}H_2O$ released in only 2.6 and 16.5 min, respectively. Interestingly, among the synthesized catalysts, Ni-La$(OH)_3$/D-MIL-125 showed the best catalytic performance (870 h^{-1}) with 100 % H_2 selectively, which is approximately 145.0, 17.4, and 1.9 times higher than those of support-free Ni NPs (6 h^{-1}), Ni-La$(OH)_3$ NPs (50 h^{-1}), and Ni/D-MIL-125 (462 h^{-1}), respectively. Moreover, the Ni-La$(OH)_3$/D-MIL-125 also showed much higher catalytic performance than Ni-La$(OH)_3$ + D-MIL-125 and Ni-La$(OH)_3$ + MIL-125 (Fig. S14). Additionally, the catalytic performance of Ni-La$(OH)_3$ + D-MIL-125 is higher than that of Ni-La$(OH)_3$ + MIL-125. The above result further reflected the important role of defects in MIL-125 for catalytic reactions. Additionally, the catalytic performances of Ni–La$(OH)_3$/D-MIL-125 catalysts prepared with different dosages of dopant La$(OH)_3$ and support MIL-125 were also studied. The optimal dosage of nLa/n(La+Ni) (Fig. S15) and MIL-125 (Fig. S16a) were 9.1 % and 70 mg, respectively. Notably, without active Ni, La$(OH)_3$/D-MIL-125 was inactive for this dehydrogenation reaction. The above results indicated that the catalytic performance of Ni-La$(OH)_3$/D-MIL-125 originates from Ni, while La$(OH)_3$ and MIL-125 act as synergists. Additionally, the dopant La$(OH)_3$ plays a critical role in the synthesis of highly efficient MIL-125-based composite catalysts. The synergistic effect at the interface of the La$(OH)_3$, Ni, and D-MIL-125 is beneficial to enhance catalytic activity, facilitating electron transfer from La$(OH)_3$ and MIL-125 to electron-rich active Ni sites, as confirmed by XPS results. Therefore, the catalytic activity of Ni-La$(OH)_3$/D-MIL-125 is significantly improved.

Since La$(OH)_3$ effectively enhanced the catalytic activity of Ni/D-MIL-125, some other metal oxides (ZrO_2, CeO_2, Y_2O_3, MnO_2) were also used as dopants in Ni/D-MIL-125. These catalysts were synthesized by the same method described for the synthesis of Ni-La$(OH)_3$/D-MIL-125, and their activities for dehydrogenation of N_2H_4 were studied and compared. As shown in Fig. 6c, it is found that all the synthesized catalysts exhibited 100% H_2 selectivity for N_2H_4 dehydrogenation and showed higher catalytic activities than that of Ni/D-MIL-125 except Ni-MnO_2/D-MIL-125. The corresponding TOF values of Ni-ZrO_2/D-MIL-125, Ni-CeO_2/D-MIL-125, Ni-Y_2O_3/D-MIL-125, Ni-MnO_2/D-MIL-125 are 760, 638, 585, and 407 h^{-1}, respectively (inset in Fig. 6c). Clearly, among these tested catalysts, Ni-La$(OH)_3$/D-MIL-125 (870 h^{-1}) displayed the highest catalytic performance. In addition, we also use other MOFs to immobilize Ni-La$(OH)_3$ NPs, such as UiO-66, ZIF-8, and ZIF-67.

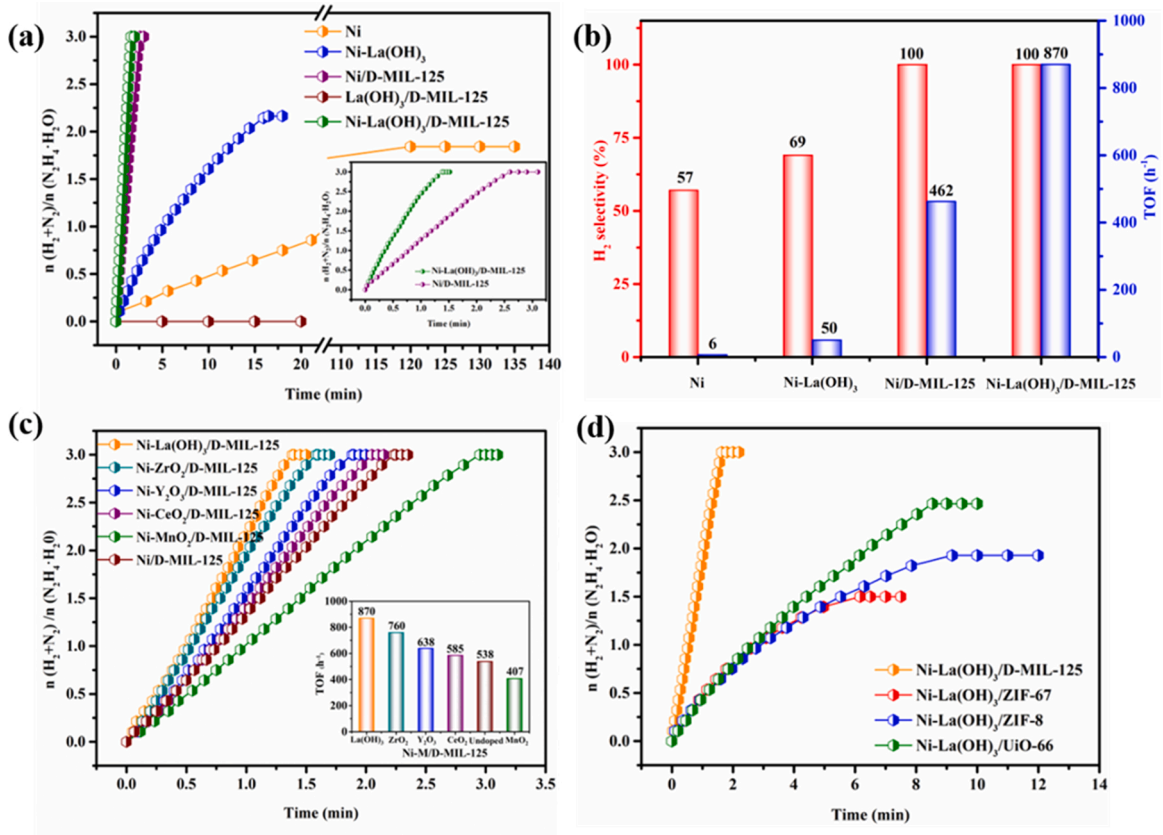

Fig. 6. (a) Time course plots for hydrogen evolution from aqueous N_2H_4 solution (0.4 M, 5 mL) and (b) the corresponding H_2 selectivity and TOF values over Ni, Ni-La(OH)$_3$, Ni/D-MIL-125, La(OH)$_3$/D-MIL-125, and Ni-La(OH)$_3$/D-MIL-125 in the presence of NaOH (3.0 M) at 343 K ($n_{Ni}/N_2H_4{\cdot}H_2O = 0.1$). Time course plots for hydrogen evolution from aqueous N_2H_4 solution over (c) Ni/D-MIL-125 doped with different metal oxides and (d) Ni-La(OH)$_3$ NPs supported on different MOFs in the presence of NaOH at 343 K. The inset of (c) showed the corresponding TOF values.

As shown in Fig. 6d and Fig. S16, compared with Ni-La(OH)$_3$/D-MIL-125, Ni-La(OH)$_3$ NPs supported on UiO-66, ZIF-8, and ZIF-67 showed much lower catalytic activity and cannot completely decompose N_2H_4 aqueous solution. Besides, the catalytic activities of Co-La(OH)$_3$/D-MIL-125, Fe-La(OH)$_3$/D-MIL-125, and Cu-La(OH)$_3$/D-MIL-125 for hydrogen production from $N_2H_4{\cdot}H_2O$ were also investigated. As shown in Fig. S17, the dehydrogenation rate of Co-La(OH)$_3$/D-MIL-125 for hydrogen production from $N_2H_4{\cdot}H_2O$ is close to that of Ni-La(OH)$_3$/D-MIL-125, but the H_2 selectivity is lower ($\alpha = 78$ %). Fe-La(OH)$_3$/D-MIL-125 can only catalyze the decomposition of $N_2H_4{\cdot}H_2O$ to produce a small amount of gas (0.4 equivalents, $\alpha = 2.5$ %), while Cu-La(OH)$_3$/D-MIL-125 has no catalytic activity for this decomposition reaction. Clearly, among all the synthesized non-noble-metal catalysts, the Ni-La(OH)$_3$/D-MIL-125 shows the highest catalytic activity and H_2 selectivity for $N_2H_4{\cdot}H_2O$ dehydrogenation. The above results further demonstrate the excellent synergy between Ni-La(OH)$_3$ NPs and D-MIL-125.

Previous literature reported that the additive NaOH played a positive role in enhancing the N_2H_4 dehydrogenation performance. Thus, the influence of NaOH concentration on the catalytic efficiency of Ni-La(OH)$_3$/D-MIL-125 was further studied. It can be observed from Fig. S18, the Ni-La(OH)$_3$/D-MIL-125 shows a low hydrogen production activity and H_2 selectivity without adding NaOH, producing only 2.0 equivalents of ($N_2 + H_2$) in 5.82 min. Surprisingly, the catalytic performance of Ni-La(OH)$_3$/D-MIL-125 is significantly enhanced by the addition of NaOH, and the best NaOH concentration is 3.0 M. However, when no catalyst is added, NaOH solution does not catalyze N_2H_4 decomposition, revealing that NaOH does not act as a catalyst, but as a promoter (Fig. S19). This promoting effect of alkali can be explained as: the OH^- ions can effectively reduce the concentration of undesired $N_2H_5^+$ ($N_2H_5^+ + OH^- \rightarrow N_2H_4 + H_2O$) and accelerate the rate-determination step to proceed ($N_2H_4 \rightarrow N_2H_3$ * + H*), thus promoting reaction kinetics. At the same time, it also can effectively prevent the generation of byproduct NH_3, improving the selectivity of hydrogen [70].

Recently, hydrazine borane ($N_2H_4BH_3$, 15.4 %) is considered to be another promising chemical hydrogen carrier because of its high hydrogen content and good stability [6,10,69]. Especially, with a suitable catalyst, hydrogen stored in $N_2H_4BH_3$ can be completely released via the hydrolysis of the BH_3 group and the decomposition of the N_2H_4 moiety, that is, 1 mol $N_2H_4BH_3$ can be released 5 mol H_2 and 1 mol N_2 ($N_2H_4BH_3(s) + 3\ H_2O \rightarrow B(OH)_3(l) + N_2(g) + 5\ H_2(g)$). In this work, the synthesized Ni-La(OH)$_3$/D-MIL-125 were subsequently applied in dehydrogenation of $N_2H_4BH_3$, in which $N_2H_4BH_3$ was synthesized according to our previous work [69] and characterized by XRD (Fig. S20). As displayed in Fig. 7a, the catalytic performances of Ni-La(OH)$_3$/D--MIL-125-x ($x = 10$–90 mg) for the catalytic dehydrogenation of $N_2H_4BH_3$ increased with the increase of the amount of reducing agent $NaBH_4$ except for Ni-La(OH)$_3$/D-MIL-125–90, which is almost consistent with the trend for N_2H_4 dehydrogenation. The catalytic efficiency of Ni-La(OH)$_3$/D-MIL-125, Ni/D-MIL-125, Ni–La(OH)$_3$ NPs, and free Ni NPs were also investigated for the dehydrogenation of $N_2H_4BH_3$. Clearly, the Ni-La(OH)$_3$/D-MIL-125 showed the highest catalytic efficiency and 100 % H_2 selectivity for $N_2H_4BH_3$ dehydrogenation (Fig. 7b), with which 6.0 equiv. of $N_2 + H_2$ can be generated in only 0.63 min at 343 K. Additionally, GC spectra showed that the produced gas contained only N_2 and H_2 (Fig. S21), further indicating a 100 % H_2 selectivity for $N_2H_4BH_3$ dehydrogenation. The TOF value of Ni-La(OH)$_3$/D-MIL-125 is calculated to be 2381 h^{-1} at 343 K, which is around 32.2, 14.4, 5.1, 3.5, and 2.3 times higher than those of the free Ni NPs (74 h^{-1}), Ni-La(OH)$_3$ NPs (165 h^{-1}), Ni-La(OH)$_3$ + MIL-125 (469 h^{-1}), Ni-La(OH)$_3$ + D-MIL-125 (682 h^{-1}), and Ni/D-MIL-125 (1035 h^{-1}) (Fig. 7c and

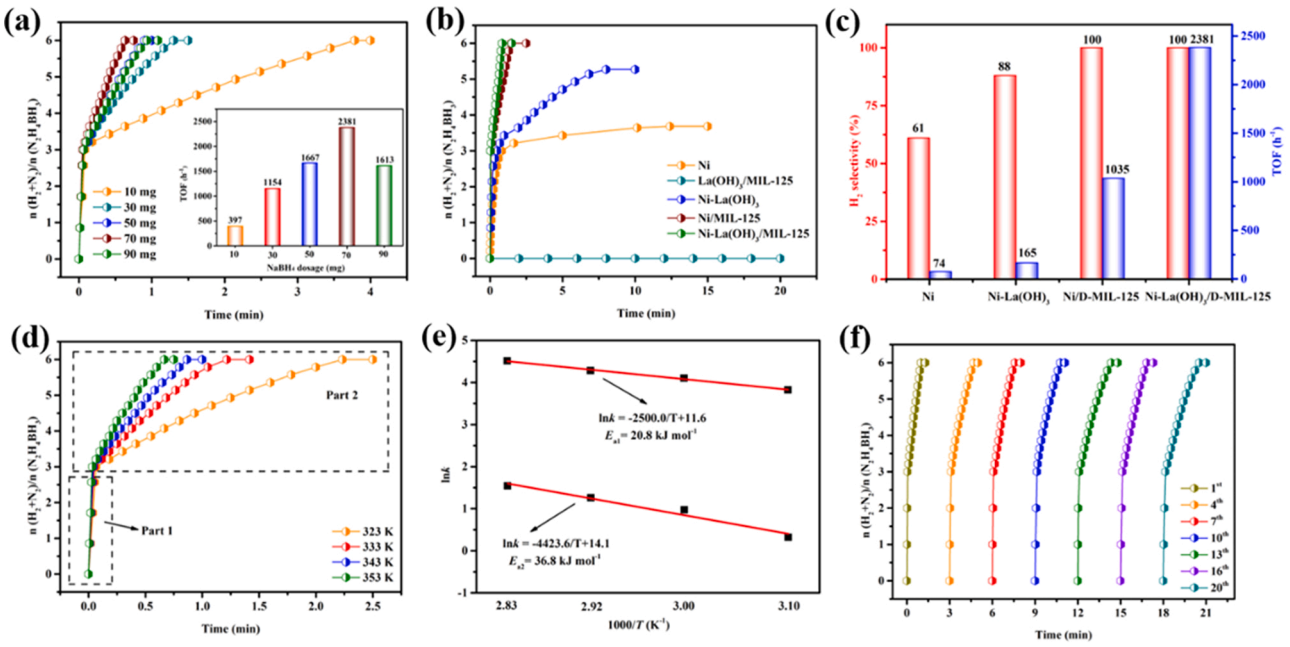

Fig. 7. Time course plots for hydrogen evolution from aqueous $N_2H_4BH_3$ solution (0.2 M, 5 mL) over (a) Ni-La(OH)$_3$/D-MIL-125-*x* (*x* = 10–90 mg) prepared with different $NaBH_4$ dosages, (b) Ni, Ni-La(OH)$_3$, Ni/D-MIL-125, La(OH)$_3$/D-MIL-125, and Ni-La(OH)$_3$/D-MIL-125 in the presence of NaOH (3.0 M) at 343 K ($n_{Ni}/N_2H_4BH_3 = 0.2$). (c) The corresponding the H_2 selectivity and TOF values. (d) Time course plots for hydrogen evolution from aqueous $N_2H_4BH_3$ solution at different temperatures, (e) the Arrhenius plot versus 1000/T, and (f) stability activity over Ni-La(OH)$_3$/D-MIL-125.

Fig. S22), respectively. Notably, the TOF value of Ni-La(OH)$_3$/D--MIL-125 is the highest among all non-noble-metal catalysts reported so far for the same dehydrogenation reaction (Table S3). The above catalytic results further indicated that defect regulation is an effective approach to improve the catalytic efficiency of catalyst, and meanwhile further illustrates the strong interaction between metal, dopant and support.

The catalytic activities of Ni-La(OH)$_3$ supported on other types of MOFs (ZIF-67, ZIF-8, and UiO-66) for $N_2H_4BH_3$ dehydrogenation were explored. As shown in Fig. S23, the catalytic activities and H_2 selectivity of Ni-La(OH)$_3$ supported on ZIF-67, ZIF-8, and UiO-66 were significantly lower than that of Ni-La(OH)$_3$/D-MIL-125, and the results were similar to that of the decomposition of $N_2H_4{\cdot}H_2O$. Additionally, the catalytic activities of Co-La(OH)$_3$/D-MIL-125, Fe-La(OH)$_3$/D-MIL-125, and Cu-La(OH)$_3$/D-MIL-125 for hydrogen production from $N_2H_4BH_3$ were also tested. As shown in Fig. S24, Co-La(OH)$_3$/D-MIL-125 has a relatively high catalytic hydrogen generation rate, but the H_2 selectivity is lower ($\beta = 70\%$). As for the Cu-La(OH)$_3$/D-MIL-125, only 3.0 equivalents of gas can be released within 0.9 min, whereas Fe-La(OH)$_3$/D-MIL-125 has the lowest catalytic activity, with a small amount of gas (1.6 equivalents) released from $N_2H_4BH_3$ within 16.3 min. Obviously, Ni-La(OH)$_3$/D-MIL-125 shows the best catalytic activity and H_2 selectively among all the synthesized non-noble-metal catalysts.

Furthermore, the effect of reaction temperature on the dehydrogenation rate of $N_2H_4BH_3$ over Ni-La(OH)$_3$/D-MIL-125 was also evaluated. As shown in Fig. 7d, the catalytic hydrogen production rate increased with increase the reaction temperature. The values of rate constant k at different temperatures were calculated from the slope of the linear part of each plot in the hydrolysis of the BH_3 group (Part 1) and the decomposition of N_2H_4 moiety (Part 2) of $N_2H_4BH_3$ from Fig. 7d. According to the Arrhenius plot of ln k versus 1000/T, the activation energy of the part 1 corresponds to the hydrolysis of BH_3 group is calculated to be 20.8 kJ mol^{-1} (E_{a1}), and the activation energy of the part 2 corresponds to the decomposition of N_2H_4 moiety is calculated to be 36.8 kJ mol^{-1} (E_{a2}). We further investigated the durability of Ni-La(OH)$_3$/D-MIL-125 catalyst for $N_2H_4BH_3$ dehydrogenation. As shown in Fig. 7f, even after 20 recycles, hydrogen production from $N_2H_4BH_3$ maintained 100% H_2 selectivity without a significant decrease in catalytic activity, indicating that the Ni-La(OH)$_3$/D-MIL-125 catalyst has good stability toward the hydrogenation of $N_2H_4BH_3$.

4. Conclusions

In summary, we have developed a facile chemical reduction method for the synthesis of defect-rich porous MIL-125 supported Ni-La(OH)$_3$ NPs. The defects in MIL-125 were in-situ generated during the chemical reduction procedure, in which Ti(IV) in part of the Ti-O cluster of MIL-125 can be reduced to Ti(III) by $NaBH_4$. Additionally, the number of defects in the catalyst can be effectively tuned by simply changing the dosage of $NaBH_4$. The resultant Ni-La(OH)$_3$/D-MIL-125 catalyst prepared with 70 mg $NaBH_4$ showed outstanding catalytic activities and 100% H_2 selectively for hydrogen production from $N_2H_4{\cdot}H_2O$ and $N_2H_4BH_3$ in an alkaline condition at 343 K, giving TOF values as high as 870 h^{-1} and 2381 h^{-1}, respectively. As far as our knowledge, the TOF value is the highest among all the reported noble-metal-free catalysts, and even exceeds some noble metal-containing catalysts. Furthermore, the Ni-La(OH)$_3$/D-MIL-125 also showed remarkable durability with no significant activity decline and metal NPs aggregation even after 20 cycles, which is helpful in promoting the practical application of $N_2H_4{\cdot}H_2O$ and $N_2H_4BH_3$ as chemical hydrogen storage materials. The enhanced performance can be attributed to the existence of abundant defective MIL-125, electron-rich, good dispersed and small Ni NPs, as well as the synergistic effect between metal and support. Importantly, this study provided a green, convenient, and low-cost defect generation strategy for MOFs, provides more ideas for the synthesis of highly efficient noble-metal-free catalysts for clean energy conversion, and broadens the vision of defect design and research.

CRediT authorship contribution statement

Jianjun Long: Conceptualization, Investigation, Formal analysis, Writing – original draft. **Qilu Yao:** Investigation, Formal analysis, Writing – review & editing. **Xiaolei Zhang**: Structure analysis. **Haochong Wu:** Formal analysis. **Zhang-Hui Lu:** Conceptualization, Writing

– review & editing, Validation, Funding acquisition, Supervision, Resources.

Declaration of Competing Interest

The authors declare that they have no known competing financial interests or personal relationships that could have appeared to influence the work reported in this paper.

Data availability

No data was used for the research described in the article.

Acknowledgment

This work was financially supported by the National Natural Science Foundation of China (Nos. 22162013 and 22162014), Natural Science Foundation of Jiangxi Province of China (No. 20212ACB204009), Sponsored Program for Academic and Technical Leaders of Major Disciplines of Jiangxi Province of China (No. 20212BCJL23059) and Sponsored Program for Cultivating Youths of Outstanding Ability in Jiangxi Normal University of China.

Appendix A. Supporting information

Supplementary data associated with this article can be found in the online version at doi:10.1016/j.apcatb.2022.121989.

References

[1] T. He, P. Pchfule, H. Wu, Q. Xu, P. Chen, Hydrogen carriers, Nat. Rev. Mater. 1 (2016) 16067.
[2] Y. Li, H.H. Wang, C. Priest, S.W. Li, P. Xu, G. Wu, Advanced electrocatalysis for energy and environmental sustainability via water and nitrogen reactions, Adv. Mater. 33 (2021), 2000381.
[3] Q.M. Sun, N. Wang, Q. Xu, J.H. Yu, Nanopore-supported metal nanocatalysts for efficient hydrogen generation from liquid-phase chemical hydrogen storage Materials, Adv. Mater. 32 (2020), 2001818.
[4] X.G. Li, Q.L. Yao, H.B. Li, Q.L. Zhu, Z.H. Lu, Porphyrin framework-derived N-doped porous carbon-confined Ru for NH_3BH_3 methanolysis: the more pyridinic-N, the better, J. Mater. Chem. A 10 (2022) 326–336.
[5] N. Wang, Q.M. Sun, T.J. Zhang, A. Mayoral, L. Li, X. Zhou, J. Xu, P. Zhang, J.H. Yu, Impregnating subnanometer metallic nanocatalysts into self-pillared zeolite nanosheets, J. Am. Chem. Soc. 143 (2021) 6905–6914.
[6] Q.L. Yao, Z.H. Lu, R. Zhang, S.L. Zhang, X.S. Chen, H.L. Jiang, A noble-metal-free nanocatalyst for highly efficient and complete hydrogen evolution from $N_2H_4BH_3$, J. Mater. Chem. A 6 (2018) 4386–4393.
[7] L. He, B.L. Liang, Y.Q. Huang, T. Zhang, Design strategies of highly selective nickel catalysts for H_2 production via hydrous hydrazine decomposition: a review, Natl. Sci. Rev. 5 (2018) 356–364.
[8] A.Q. Zhang, J.H. Xia, Q.L. Yao, Z.H. Lu, Pd–WO_x heterostructures immobilized by MOFs-derived carbon cage for formic acid dehydrogenation, Appl. Catal. B Environ. 309 (2022), 121278.
[9] X.R. Li, X.C. Yang, H.G. Xue, H. Pang, Q. Xu, Metal–organic frameworks as a platform for clean energy applications, EnergyChem 2 (2020), 100027.
[10] W. Wei, X.L. Hong, Q.L. Yao, Z.H. Lu, Bimetallic Ni–Pt nanoparticles immobilized on mesoporous N-doped carbon as a highly efficient catalyst for complete hydrogen evolution from hydrazine borane, J. Mater. Chem. A 8 (2020) 13694–13701.
[11] S.J. Li, X. Kang, B.R. Wulan, X.L. Qu, K. Zheng, X.D. Han, J.M. Yan, Noble-metal-free Ni-MoO_x nanoparticles supported on BN as a highly efficient catalyst toward complete decomposition of hydrazine borane, Small 2 (2018), 1800250.
[12] M. Li, J.X. Sun, G. Chen, S. Wang, S.Y. Yu, Inducing photocarrier separation via 3D porous faveolate cross-linked carbon to enhance photothermal/pyroelectric property, Adv. Powder Mater. 1 (2022), 100032.
[13] S.K. Singh, Q. Xu, Nanocatalysts for hydrogen generation from hydrazine, Catal. Sci. Technol. 3 (2013) 1889–1900.
[14] Y.X. Cheng, X. Wu, H.L. Xu, Catalytic decomposition of hydrous hydrazine for hydrogen production, Sustain. Energy Fuels 3 (2019) 343–365.
[15] C.G. Lang, Y. Jia, X.D. Yao, Recent advances in liquid-phase chemical hydrogen storage, Energy Storage Mater. 26 (2020) 290–312.
[16] Q.L. Zhu, Q. Xu, Liquid organic and inorganic chemical hydrides for high-capacity hydrogen storage, Energy Environ. Sci. 5 (2015) 478–512.
[17] Q.L. Yao, Y.Y. Ding, Z.H. Lu, Noble-metal-free nanocatalysts for hydrogen generation from boron- and nitrogen-based hydrides, Inorg. Chem. Front. 7 (2020) 3837–3874.
[18] A.Q. Zhang, Q.L. Yao, Z.H. Lu, Recent progress on catalysts for hydrogen evolution from decomposition of hydrous hydrazine, Acta Chim. Sin. 79 (2021) 885–902.
[19] C. Wan, L. Sun, L.X. Xu, D.G. Cheng, F.Q. Chen, X.L. Zhan, Y.R. Yang, Novel NiPt alloy nanoparticle decorated 2D layered g-C_3N_4 nanosheets: A highly efficient catalyst for hydrogen generation from hydrous hydrazine, J. Mater. Chem. A 7 (2019) 8798–8804.
[20] K. Wang, Q.L. Yao, S.J. Qing, Z.H. Lu, $La(OH)_3$ nanosheet-supported CoPt nanoparticles: a highly efficient and magnetically recyclable catalyst for hydrogen production from hydrazine in aqueous solution, J. Mater. Chem. A 7 (2019) 9903–9911.
[21] Y.P. Qiu, L.L. Zhou, Q. Shi, P. Wang, Free-standing Pt–Ni nanowires catalyst for H_2 generation from hydrous hydrazine, Chem. Commun. 57 (2021) 623–626.
[22] D. Bhattacharjee, S. Dasgupta, Trimetallic NiFePd nanoalloy catalysed hydrogen generation from alkaline hydrous hydrazine and sodium borohydride at room temperature, J. Mater. Chem. A 3 (2015) 24371–24378.
[23] X. Song, P. Yang, J.C. Wang, X.C. Zhao, Y.L. Zhou, Y.T. Li, L.J. Yang, NiFePd/UiO-66 nanocomposites as highly efficient catalysts to accelerate hydrogen evolution from hydrous hydrazine, Inorg. Chem. Front. 6 (2019) 2727–2735.
[24] L. He, B.L. Liang, L. Li, X.F. Yang, Y.Q. Huang, A.Q. Wang, X.D. Wang, T. Zhang, Cerium-oxide-modified nickel as a non-noble metal catalyst for selective decomposition of hydrous hydrazine to hydrogen, ACS Catal. 5 (2015) 1623–1628.
[25] Y.P. Qiu, Q. Shi, L.L. Zhou, M.H. Chen, C. Chen, P.P. Tang, G.S. Walker, P. Wang, NiPt nanoparticles anchored onto hierarchical nanoporous N-doped carbon as an efficient catalyst for hydrogen generation from hydrazine monohydrate, ACS Appl. Mater. Interfaces 12 (2020) 18617–18624.
[26] F.Z. Song, X.C. Yang, Q. Xu, Ultrafine bimetallic Pt–Ni nanoparticles achieved by metal–organic framework templated zirconia/porous carbon/reduced graphene oxide: Remarkable catalytic activity in dehydrogenation of hydrous hydrazine, Small Methods 4 (2019), 1900707.
[27] A. Kumar, X.C. Yang, Q. Xu, Ultrafine bimetallic Pt–Ni nanoparticles immobilized on 3-dimensional N-doped graphene networks: a highly efficient catalyst for dehydrogenation of hydrous hydrazine, J. Mater. Chem. A 7 (2019) 112–115.
[28] S.K. Singh, Q. Xu, Complete conversion of hydrous hydrazine to hydrogen at room temperature for chemical hydrogen storage, J. Am. Chem. Soc. 131 (2009) 18032–18033.
[29] J. Wang, X.B. Zhang, Z.L. Wang, Y. Zhang, Rhodium–nickel nanoparticles grown on graphene as highly efficient catalyst for complete decomposition of hydrous hydrazine at room temperature for chemical hydrogen storage, Energy Environ. Sci. 5 (2012) 6885–6888.
[30] S.K. Singh, A.K. Singh, K. Aranishi, Q. Xu, Noble-metal-free bimetallic nanoparticle-catalyzed selective hydrogen generation from hydrous hydrazine for chemical hydrogen storage, J. Am. Chem. Soc. 133 (2011) 19638–19641.
[31] L. He, Y.Q. Huang, A.Q. Wang, X.D. Wang, X.W. Chen, J.J. Delgado, T. Zhang, A noble-metal-Free catalyst derived from Ni-Al hydrotalcite for hydrogen generation from $N_2H_4{\cdot}H_2O$ decomposition, Angew. Chem. Int. Ed. 51 (2012) 6191–6194.
[32] J.J. Zhang, K. Kang, Z.Q. Yang, H.B. Dai, D.W. Zhuang, P. Wang, A cost-effective NiMoB–$La(OH)_3$ catalyst for hydrogen generation from decomposition of alkaline hydrous hydrazine solution, J. Mater. Chem. A 1 (2013) 11623–11628.
[33] K.V. Manukyan, A. Cross, S. Rouvimov, J. Miller, A.S. Mukasyan, E.E. Wolf, Low temperature decomposition of hydrous hydrazine over FeNi/Cu nanoparticles, Appl. Catal. A 476 (2014) 47–53.
[34] J. Wang, Y. Li, Y. Zhang, Precious-metal-free nanocatalysts for highly efficient hydrogen production from hydrous hydrazine, Adv. Funct. Mater. 24 (2014) 7073–7077.
[35] H.T. Zou, S.L. Zhang, X.L. Hong, Q.L. Yao, Y. Luo, Z.H. Lu, Immobilization of Ni–Pt nanoparticles on MIL-101/rGO composite for hydrogen evolution from hydrous hydrazine and hydrazine borane, J. Alloy. Compd. 835 (2020), 155426.
[36] P.P. Zhao, N. Cao, W. Luo, G.Z. Cheng, Nanoscale MIL-101 supported RhNi nanoparticles: an efficient catalyst for hydrogen generation from hydrous hydrazine, J. Mater. Chem. A 3 (2015) 12468–12475.
[37] S.K. Singh, Q. Xu, Bimetallic nickel-iridium nanocatalysts for hydrogen generation by decomposition of hydrous hydrazine, Chem. Commun. 46 (2010) 6545–6547.
[38] L. He, Y.Q. Huang, X.Y. Liu, L. Li, A.Q. Wang, X.D. Wang, C.Y. Mou, T. Zhang, Structural and catalytic properties of supported Ni–Ir alloy catalysts for H_2 generation via hydrous hydrazine decomposition, Appl. Catal. B Environ. 147 (2014) 779–788.
[39] X.L. Hong, Q.L. Yao, M.L. Huang, H.X. Du, Z.H. Lu, Bimetallic NiIr nanoparticles supported on lanthanum oxy-carbonate as highly efficient catalysts for hydrogen evolution from hydrazine borane and hydrazine, Inorg. Chem. Front. 6 (2019) 2271–2278.
[40] W. Kang, A. Varma, Hydrogen generation from hydrous hydrazine over Ni/CeO_2 catalysts prepared by solution combustion synthesis, Appl. Catal. B Environ. 220 (2018) 409–416.
[41] H.L. Wang, J.M. Yan, S.J. Li, X.W. Zhang, Q. Jiang, Noble-metal-free NiFeMo nanocatalyst for hydrogen generation from the decomposition of hydrous hydrazine, J. Mater. Chem. A 3 (2015) 121–124.
[42] D.D. Wu, M. Wen, C. Gu, Q.S. Wu, 2D NiFe/CeO_2 basic-site-enhanced catalyst via in-situ topotactic reduction for selectively catalyzing the H_2 generation from $N_2H_4{\cdot}H_2O$, ACS Appl. Mater. Interfaces 9 (2017) 16103–16108.
[43] H. Yen, Y. Seo, S. Kaliaguine, F. Kleitz, Role of metal-support interactions, particle size, and metal-metal synergy in CuNi nanocatalysts for H_2 generation, ACS Catal. 5 (2015) 5505–5511.
[44] J.M. Chen, H.T. Zou, Q.L. Yao, M.H. Luo, X.G. Li, Z.H. Lu, Cr_2O_3-modified NiFe nanoparticles as a noble-metal-free catalyst for complete dehydrogenation of hydrazine in aqueous solution, Appl. Surf. Sci. 501 (2020), 144247.

[45] X.L. Hong, Q.L. Yao, J.J. Long, X.G. Li, X.S. Chen, Z.H. Lu, CuNi/$La_2O_2CO_3$/rGO nanocomposites: An efficient noble-metal-free catalyst for hydrogen evolution from $N_2H_4{\cdot}H_2O$, Ind. Eng. Chem. Res. 60 (2021) 16224–16232.
[46] H.F. Wang, L.M. Wu, A.Z. Jia, X.N. li, Z.T. Shi, M.M. Duan, Y.J. Wang, Ni nanoparticles encapsulated in the channel of titanate nanotubes: efficient noble-metal-free catalysts for selective hydrogen generation from hydrous hydrazine, Chem. Eng. J. 322 (2018) 637–646.
[47] W. Kang, H. Guo, A. Varma, Noble-metal-free NiCu/CeO_2 catalysts for H_2 generation from hydrous hydrazine, Appl. Catal. B Environ. 249 (2019) 54–62.
[48] W. Gao, C.M. Li, H. Chen, M. Wu, S. He, M. Wei, D.G. Evans, X. Duan, Supported nickel–iron nanocomposites as a bifunctional catalyst towards hydrogen generation from $N_2H_4{\cdot}H_2O$, Green Chem. 16 (2014) 1560–1568.
[49] J. Wang, Y. Li, Y. Zhang, Precious-metal-free nanocatalysts for highly efficient hydrogen production from hydrous hydrazine, Adv. Funct. Mater. 24 (2014) 7073–7077.
[50] X.B. Hong, Z.K. Han, X.J. Xu, D. Sarker, J. Zhou, M. Wu, Z.C. Liu, M.H. Huang, H. Q. Jiang, Controllable amorphization engineering on bimetallic metal–organic frameworks for ultrafast oxygen evolution reaction, Chem. Eng. J. 418 (2021), 129330.
[51] X.Y. Zheng, C. Jia, G.Z. Fan, W.J. Luo, Z.S. Li, Z.G. Zou, Modulation of disordered coordination degree based on surface defective metal–organic framework derivatives toward boosting oxygen evolution electrocatalysis, Small 16 (2020), 2003630.
[52] X. Ma, L. Wang, Q. Zhang, H.L. Jiang, Switching on the photocatalysis of metal–organic frameworks by engineering structural defects, Angew. Chem. Int. Ed. 58 (2019) 12175–12179.
[53] X.Y. Yuan, L.F. Li, Z.N. Shi, H. Liang, S.H. Li, Z.W. Qiao, Molecular-fingerprint machine-learning-assisted design and prediction for high-performance MOFs for capture of NMHCs from air, Adv. Powder Mater. 1 (2022), 100026.
[54] I.A. Lázaro, H. Szalad, P. Valiente, J. Albero, H. Garcia, C.M. Gastaldo, Tuning the photocatalytic activity of Ti-based metal–organic frameworks through modulator defect-engineered functionalization, ACS Appl. Mater. Interfaces 14 (2022) 21007–21017.
[55] S.J. Li, H.L. Wang, B.R. Wulan, Z.X. Bo, J.M. Yan, Q. Jiang, Complete dehydrogenation of $N_2H_4BH_3$ over noble-metal-free $Ni_{0.5}Fe_{0.5}$–CeO_x/MIL-101 with high activity and 100% electivity, Adv. Energy Mater. 21 (2018), 1800625.
[56] R.N. Yang, S.M. Peng, B. Lan, M. Sun, Z.H. Zou, C.Y. Sun, Z.H. Gao, G.C. Xing, L. Yu, Oxygen defect engineering of β-MnO_2 catalysts via phase transformation for selective catalytic reduction of NO, Small 17 (2021), 2102408.
[57] Z.L. Fang, B. Bueken, D.E.D. Vos, R.A. Fischer, Defect-engineered metal–organic frameworks, Angew. Chem. Int. Ed. 54 (2015) 7234–7254.
[58] W.L. Xiang, Y.P. Zhang, Y.F. Chen, C.J. Liu, X. Tu, Synthesis, characterization and application of defective metal–organic frameworks: current status and perspectives, J. Mater. Chem. A 8 (2020) 21526–21546.
[59] N.X. Li, X.C. Liu, J.C. Zhou, W.S. Chen, M.C. Liu, Encapsulating CuO quantum dots in MIL-125(Ti) coupled with g-C_3N_4 for photocatalytic CO_2 reduction, Chem. Eng. J. 399 (2020), 125782.
[60] Y. Yamazaki, K. Mori, Y. Kuwahara, H. Kobayashi, H. Yamashita, Defect engineering of Pt/TiO_{2-x} photocatalysts via reduction treatment assisted by hydrogen spillover, ACS Appl. Mater. Interfaces 13 (2021) 48669–48678.
[61] P.V. Hlophe, L.C. Mahlalela, L.N. Dlamini, Composite of platelet-like orientated $BiVO_4$ fused with MIL-125(Ti): synthesis and characterization, Sci. Rep. 9 (2019), 10044.
[62] K.H. Li, Y.B. Liu, F. Li, C.S. Shen, Y.V. Kaneti, Y. Yamauchi, B. Yuliarto, B. Chen, C. C. Wang, Defect-rich hierarchical porous UiO-66(Zr) for tunable phosphate removal, Environ. Sci. Technol. 55 (2021) 13209–13218.
[63] X.L. Song, Y. Wang, T. Zhu, J.L. Liu, S.W. Zhang, Facile synthesis a novel core–shell amino functionalized MIL-125(Ti) micro-photocatalyst for enhanced degradation of tetracycline hydrochloride under visible light, Chem. Eng. J. 416 (2021), 129126.
[64] Y. Zhang, G. Li, L.H. Kong, H. Lu, Deep oxidative desulfurization catalyzed by Ti-based metal-organic frameworks, Fuel 219 (2018) 103–110.
[65] Z. Guo, J.X. Wang, Y. Muhammad, Y.B. Zhang, S.J. Shah, Y. Hu, Z. Chu, Z.X. Zhao, Z.X. Zhao, Enhanced moisture-resistance and excellent photocatalytic performance of synchronous N/Zn-decorated MIL-125(Ti) for vaporous acetaldehyde degradation, Chem. Eng. J. 388 (2020), 124389.
[66] O. Song-Il, J.M. Yan, H.L. Wang, Z.L. Wang, Q. Jiang, Ni/La_2O_3 catalyst containing low content platinum–rhodium for the dehydrogenation of $N_2H_4{\cdot}H_2O$ at room temperature, J. Power Sources 262 (2014) 386–390.
[67] H.T. Zou, F. Guo, M.H. Luo, Q.L. Yao, Z.H. Lu, La$(OH)_3$-decorated NiFe nanoparticles as efficient catalyst for hydrogen evolution from hydrous hydrazine and hydrazine borane, Int. J. Hydrog. Energy 45 (2020) 11641–11650.
[68] K. Yang, K.K. Yang, S.L. Zhang, Y. Luo, Q.L. Yao, Z.H. Lu, Complete dehydrogenation of hydrazine borane and hydrazine catalyzed by MIL-101 supported NiFePd nanoparticles, J. Alloy. Compd. 732 (2018) 363–371.
[69] Z.J. Zhang, Z.H. Lu, H.L. Tan, X.S. Chen, Q.L. Yao, CeO_x-modified RhNi nanoparticles grown on rGO as highly efficient catalysts for complete hydrogen generation from hydrazine borane and hydrazine, J. Mater. Chem. A 3 (2015) 23520–23529.
[70] Y.X. Cheng, X. Wu, H.L. Xu, Catalytic decomposition of hydrous hydrazine for hydrogen production, Sustain. Energy Fuels 3 (2019) 343–365.